crystals

MDPI

Article

Synthesis and Characterization of New $Sr_3(BO_3)_2$ Crystal for Stimulated Raman Scattering Applications

Xinle Wang, Hongwei Qi, Yanlu Li, Fapeng Yu *, Hewei Wang, Feifei Chen, Yanqing Liu, Zhengping Wang *, Xinguang Xu and Xian Zhao

Institute of Crystal Materials & Key Laboratory of Functional Crystal Materials and Devices, Shandong University, Jinan 250100, China; sinyerwang@foxmail.com (X.W.); xzonepiece@163.com (H.Q.); liyanlu@sdu.edu.cn (Y.L.); wang_hewei@126.com (H.W.); ffchen2013@126.com (F.C.); yanqingliu126yx@126.com (Y.L.); xgxu@sdu.edu.cn (X.X.); xianzhao@sdu.edu.cn (X.Z.)

* Correspondence: fapengyu@sdu.edu.cn (F.Y.); zpwang@sdu.edu.cn (Z.W.); Tel.: +86-531-8836-4330 (F.Y.)

Academic Editor: Shujun Zhang

Received: 10 March 2017; Accepted: 24 April 2017; Published: 28 April 2017

Abstract: A new kind of borate crystalline material $Sr_3(BO_3)_2$ with a similar calcite type structure was designed and synthesized by solid state reaction method, moreover, the single crystal growth was attempted with traditional Czochralski pulling method. Crystal phase of $Sr_3(BO_3)_2$ was investigated by using X-Ray powder diffraction (XRPD) at room temperature and found similar to $Ca_3(BO_3)_2$ crystal with space group of R-3c. The phase stability was studied by means of thermogravimetric differential thermal analysis (TG/DTA) and high temperature XRPD up to 1350 °C, where an obvious endothermic peak was observed in DTA curve around 1250 °C, and weak splits of diffraction peaks were found at temperatures above 1250 °C, indicating the existence of structure transformation for $Sr_3(BO_3)_2$ crystal. Raman properties were studied experimentally and theoretically by using density functional perturbation theory, though the strongest frequency shift of $Sr_3(BO_3)_2$ crystal (900 cm^{-1}) was comparable to that of $Ca_3(BO_3)_2$ (927 cm^{-1}), the line width of the strongest Raman peak obtained for $Sr_3(BO_3)_2$ (5.72 cm^{-1}) was much lower than $Ca_3(BO_3)_2$ (7.01 cm^{-1}), indicating a larger Raman gain for $Sr_3(BO_3)_2$ crystal, which would be favorable for stimulated Raman scattering application.

Keywords: $Sr_3(BO_3)_2$; Raman; crystal growth; phase transformation

1. Introduction

As one of the earliest nonlinear optical processes, in recent years, stimulated Raman scattering (SRS) has become an important and efficient method for frequency conversion to fulfill various applications including optical molecular imaging, structure analysis, biology monitoring, and medical treatment [1–7]. Different from the optical frequency doubling, SRS is a third-order nonlinear optical process with many advantages such as larger angular acceptance, and no walk-off angle and phase-matching (PM) direction [8]. In the early years, SRS experiments were mostly based on liquids and gases including CH_4, N_2, and benzene etc. [9]. However, some flaws such as poisonousness and instability restrict their application in SRS. Besides the liquids and gases SRS mediums, solid materials, especially crystals, were applied in SRS. Since the 1980s, several new artificial crystals—Such as $Ba(NO_3)_2$, $BaWO_4$ and YVO_4 crystals—Have been studied for SRS applications [10–15]. These crystals were revealed to possess many merits for SRS process, including larger Raman gain coefficient, stable thermal and mechanical properties, good chemical stability, non-deliquescence, and small volume etc. However, the relatively low anti-optical damage threshold and the long cut-off wavelength restricted their applications for SRS in the ultraviolet waveband [16,17].

SRS is an inelastic scattering process with inevitable energy loss. Therefore, both the Raman gain coefficient and the anti-optical damage threshold are critical parameters for selecting Raman

crystals [18]. Among the artificial crystal materials, borate crystals are famous for laser application in deep ultraviolet due to the high anti-optical damage threshold and high transmittance in a wide transmission spectrum. In the borate series crystals, the calcite phase $Ca_3(BO_3)_2$ crystal with point group-3m (space group R-3c) was reported to be promising for SRS application from deep ultraviolet to near infrared [18]. However, the SRS performance could see further improvement. In general, a cation with larger ionic radius would be beneficial in inducing a larger Raman gain in crystals with a certain structure. Taking the reported AWO_4 (A = Ca, Sr and Ba) type crystals for instance, the $BaWO_4$ crystal was found to possess better Raman properties than $SrWO_4$ and $CaWO_4$ crystals, such as more narrow line width (2.2, 2.7, and 4.8 cm^{-1} for $BaWO_4$, $SrWO_4$, and $CaWO_4$ crystals, respectively), larger Raman gain (8.5, 5.0, and 3.0 cm/GW @1064 nm for $BaWO_4$, $SrWO_4$, and $CaWO_4$ crystals, respectively), and larger Raman shift (926, 922, and 908 cm^{-1} for $BaWO_4$, $SrWO_4$, and $CaWO_4$ crystals, respectively) [19–21]. Hence, it is interesting and necessary to discuss and compare the Raman properties of $Ca_3(BO_3)_2$ type crystals, including $Ca_3(BO_3)_2$, $Mg_3(BO_3)_2$, and $Sr_3(BO_3)_2$. However, only $Ca_3(BO_3)_2$ has been studied up to date [18].

According to the Goldschmidt's Rules [22], it might be possible to substitute an ion in polyhedron with another ion with the same valence and low discrepancy of ionic radius (<15%). As far as $Ca_3(BO_3)_2$ type crystals are concerned, though the magnesium (Mg), strontium (Sr), and Barim (Ba) belong to the IIA elements, only the Sr ($r^{Sr(+2)}$ = 1.12 Å [23]) possess comparable ionic radius to that of Ca^{2+} ($r^{Ca(+2)}$ = 1.00 Å [23]), while the Mg^{2+} and Ba^{2+} show a large ionic radius discrepancy over 15%. Additionally, it had been known that the crystal symmetry of $Mg_3(BO_3)_2$ grown by Czochralski (Cz) method was orthorhombic (space group P*nmn* and point group *mmm*) [24], different to the trigonal $Ca_3(BO_3)_2$ crystal. In contrast, the $Sr_3(BO_3)_2$ was reported to be trigonal and share the same crystal symmetry with $Ca_3(BO_3)_2$ [25]. In order to evaluate the SRS properties of $Sr_3(BO_3)_2$, the single crystal growth was attempted and related properties were characterized in this work.

2. Structure Analysis and New Crystal Design

The $Sr_3(BO_3)_2$ was first reported by Richter and Müller in 1980, and revealed to belong to trigonal system and R-3c space group (ICSD No. 93395) [25], and the lattice parameters were reported to be $a = b = 9.046$ Å and $c = 12.566$ Å [26]. Figure 1 presents the crystal structure of $Sr_3(BO_3)_2$, where the $[BO_3]^{3-}$ group were observed to form a regular triangle in the same plane normal to the crystallographic *c*-axis, and the three terminal oxygen atoms were linked with Sr atoms, which were similar to $Ca_3(BO_3)_2$ crystal (Figure 1a,b). It can be observed from Figure 1c,d that the $[BO_3]^{3-}$ groups were parallel to each other. The twisty Sr-O octahedron and the triangular $[BO_3]^{3-}$ group were shown in Figure 1e,f, respectively. It was noticed that the $Mg_3(BO_3)_2$ crystal belongs to the P*nmn* space group (point group *mmm*), and the lattice parameters were reported to be $a = 5.4014$ Å, $b = 8.4233$ Å, $c = 4.5071$ Å, $\alpha = \beta = \gamma = 90°$, and $V = 205.1$ $Å^3$ [27]. It can be presumed that the variation of ionic radius resulted in the change of lattice parameters, leading to the structure transformation from trigonal to orthorhombic when the ion varied from Sr^{2+} to Mg^{2+}.

The potential Raman properties of $Mg_3(BO_3)_2$, $Ca_3(BO_3)_2$, and $Sr_3(BO_3)_2$ crystals were theoretically studied within the framework of density functional perturbation theory by using the Cambridge Sequential Total Energy Package (CASTEP) code [28]. The exchange and correlation potential were described in a generalized gradient approximation of Perdew-Burke-Erenzerhof functionality (GGA-PBE) [29], and the interaction between the valence electrons and the core electrons was described by norm-conserving pseudopotentials [30]. The cutoff energy and Monkhorst-Pack *k*-point were set to 380 eV and 4 × 4 × 4. The primitive cells containing 22 atoms were used to reduce the computational cost. All the configurations were fully optimized before the Raman spectrum calculation with the error of *a* and *c* lattices within 2%. As it can be observed in Figure 2, the strongest Raman shifts for $Mg_3(BO_3)_2$, $Ca_3(BO_3)_2$, and $Sr_3(BO_3)_2$ crystals appeared at 895, 909, and 886 cm^{-1}, respectively, associated with the symmetrical stretching vibration of $[BO3]^{3-}$ group. It was noticed that the $Ca_3(BO_3)_2$ and $Sr_3(BO_3)_2$ crystals showed more plentiful peaks than $Mg_3(BO_3)_2$, which might be

associated with their different crystal structures, as both the $Ca_3(BO_3)_2$ and $Sr_3(BO_3)_2$ crystals belong to the same space group R-3c, while $Mg_3(BO_3)_2$ belongs to space group P*nmn*. The plentiful peaks of $Ca_3(BO_3)_2$ and $Sr_3(BO_3)_2$ crystals would be beneficial for achieving applicable wavelengths in the field of SRS.

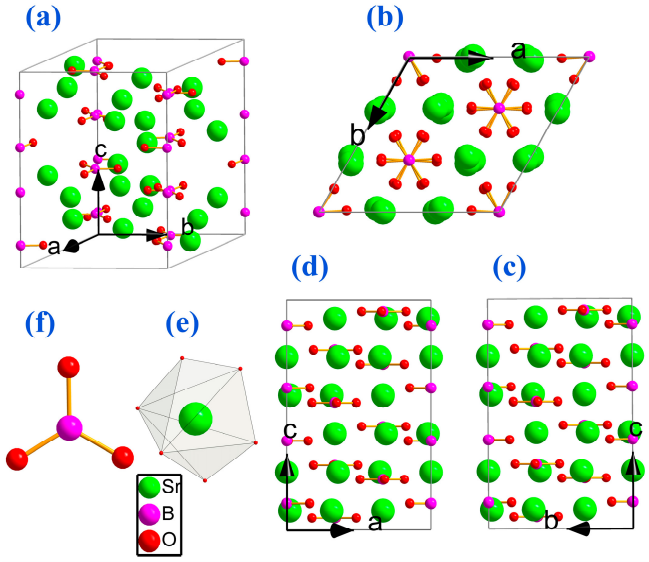

Figure 1. Schematic of $Sr_3(BO_3)_2$ crystal structure. (**a**) Main view; (**b**) *c*-axes view; (**c**) *a*-axes view; (**d**) *b*-axes view; (**e**) Sr-O octahedron and (**f**) $[BO_3]^{3-}$ group.

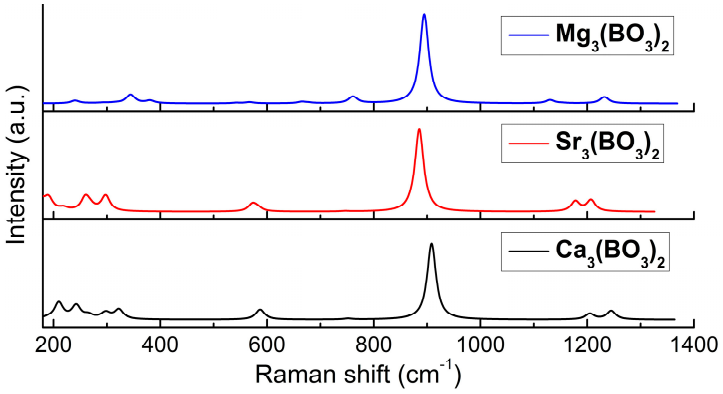

Figure 2. The theoretical Raman frequency shifts for $Mg_3(BO_3)_2$, $Ca_3(BO_3)_2$ and $Sr_3(BO_3)_2$ crystals.

3. Experimental

The polycrystalline $Sr_3(BO_3)_2$ was prepared by using solid state reaction method, where the starting materials were $SrCO_3$ (99.95%) and H_3BO_3 (99.99%) powders, which were weighed in stoichiometric ratio, according to the chemical reaction equation below,

$$3SrCO_3 + 2H_3BO_3 = Sr_3(BO_3)_2 + 3CO_2\uparrow + 3H_2O$$

In order to compensate the evaporation of B_2O_3 during the solid-state reaction and crystal growth processes, an excess of H_3BO_3 (1.0 wt %) was added to the starting materials. All the starting materials were fully mixed for at least 24 h to ensure homogeneity. Then mixed raw materials were sintered at 1000 °C for 10 h to decompose H_3BO_3 and $SrCO_3$ completely. After that the sintered raw materials were ground, mixed again and pressed into pieces, which were charged into an alumina crucible and sintered at 1250 °C for at least 40 h to synthesize the polycrystalline $Sr_3(BO_3)_2$.

A J40 single crystal growth furnace was used to grow $Sr_3(BO_3)_2$ single crystal. The prepared polycrystalline $Sr_3(BO_3)_2$ blocks were put into an Ir crucible (ø60mm) in the furnace, where the atmosphere was controlled to be a mixture of 2 vol % air and 98 vol % N_2. It is important to find out the melting point of $Sr_3(BO_3)_2$ in the first run, so the heating rate was kept slow enough when the floating compounds on the melt got shrinking. The melt was maintained at 50 °C higher than the observed melting point for several hours to make the melt homogeneous. Then the temperature was slowly decreased for seeding. $Ca_3(BO_3)_2$ crystal seed along the *c*-axis was used to grow $Sr_3(BO_3)_2$ single crystal. It was found that the melting point of $Sr_3(BO_3)_2$ crystal was higher than $Ca_3(BO_3)_2$ (1470 °C [31]), so the seeding process was carried out within a short period in order to get rid of seed fusing. During the crystal growth, the pulling rate was controlled at 0.4 mm/h and the rotation rate was varied from 15 to 20 rmp. For the purpose of decreasing the thermal stress in as-grown crystal, a long period (~100 h) was implemented to cool down the $Sr_3(BO_3)_2$ crystal to room temperature.

The thermogravimetric and differential thermal analysis (TG-DTA) for $Sr_3(BO_3)_2$ was carried out with a Diamond TMA thermal mechanical analyzer, provided by Perkin Elmer Corporation. The heating rate was 10 °C/min and the flow rate of N_2 was 50 mL/min.

In order to study the crystal structure and possible phase transition of $Sr_3(BO_3)_2$, the synthesized polycrystalline $Sr_3(BO_3)_2$ and the grown $Sr_3(BO_3)_2$ crystal blocks were selected for X-ray Powder Diffraction (XRPD) characterization (Bruker D8 Advance X-Ray Diffractometer equipped with Cu-Kα radiation and a semiconductor array detector (Bruker LynxEye)). High temperature structure analysis for $Sr_3(BO_3)_2$ crystal was carried out by using an in situ XRPD equipped with a high temperature in situ attachment (Anton Paar HTK-2000N). The tested temperature was operated from 1150 °C to 1350 °C, and the diffraction spectra were recorded with step of 50 °C. The heating rate was controlled to be 10 °C/min and the retention time at each desired temperature was 5 min.

The powder Raman spectra of the grown $Sr_3(BO_3)_2$ crystal obtained by Cz method was measured from 20 to 7500 cm^{-1} by an FT-IR & Raman Spectrograph (NEXUS 670) with a high resolution of 0.09 cm^{-1}. The used exciting source was a 1064 nm laser pumped by a Nd:YVO_4 crystal.

4. Results and Discussion

4.1. Single Crystal Growth

The $Sr_3(BO_3)_2$ crystal was grown by using Cz-pulling method. It was observed that the $Sr_3(BO_3)_2$ crystal was transparent in the furnace after pulling out of the melt, however, crystal cracks slowly emerged during the following cooling process. As crystal cracks spread, the $Sr_3(BO_3)_2$ crystal was finally broken into pieces, as shown in Figure 3. This phenomenon always occurred no matter how the component or temperature gradient was adjusted.

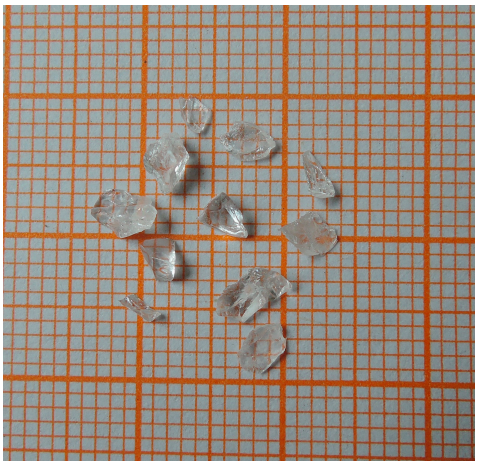

Figure 3. The obtained $Sr_3(BO_3)_2$ crystal pieces.

4.2. Thermogravimetric and Differential Thermal Analysis

The thermogravimetric and differential thermal analysis were measured from 20 °C to 1350 °C. Figure 4 gives the measured TG-DTA curves, where the mass loss was less than 0.6% over the tested temperature range (the red line in Figure 4) and an endothermic peak in DTA curve (the blue line in Figure 4) was observed at around 1250 °C. According to previous reports, the melting point for $Ca_3(BO_3)_2$ was 1479 °C [31], higher than 1285 °C for $Sr_3(BO_3)_2$ [32]. However, in this work, the melting point for $Sr_3(BO_3)_2$ was judged to be higher than $Ca_3(BO_3)_2$, since the $Ca_3(BO_3)_2$ crystal seed melted rapidly when dipped into the $Sr_3(BO_3)_2$ melt during the seeding process. Therefore, the endothermic peak observed at round 1250 °C was presumed to be associated with a phase transition.

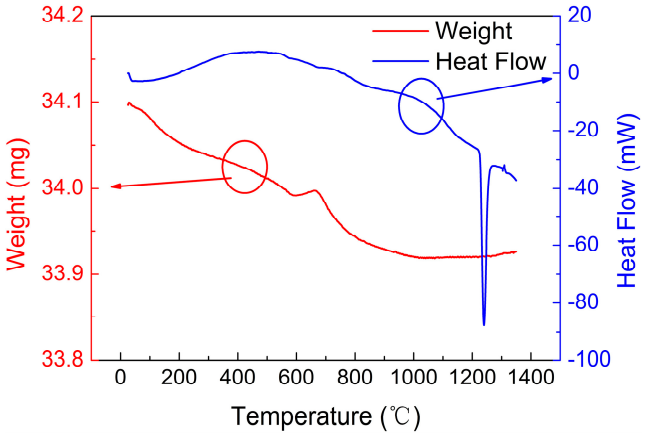

Figure 4. TG-DTA curves of $Sr_3(BO_3)_2$ crystal samples.

4.3. Structure and Phase Transition Analysis

Figure 5 shows the XRPD pattern of as-grown $Sr_3(BO_3)_2$ crystals as well as that of polycrystalline sample prepared by solid state reaction for comparison, where all the refraction peaks of the as-grown bulk crystal sample and polycrystalline sample were in consistent with the standard diffraction data (JCPDS No. 31–1343), indicating the $Sr_3(BO_3)_2$ samples before and after Cz growth possess the same crystal phase. The cell parameters for $Sr_3(BO_3)_2$ crystals were analyzed utilizing Jade Version 6 with necessary steps including phase retrieval, subtracting the background and stripping the Kα2-lines with cubic spline, smoothing and fitting all profiles [33]. In the end, the cell parameters were obtained to be $a = b = 9.02895(0.002125)$ Å, $c = 12.54646(0.002462)$ Å, $\alpha = \beta = 90°$, $\gamma = 120°$, and $V = 885.78(4.72)$ Å^3, slightly lower than the reported values [26].

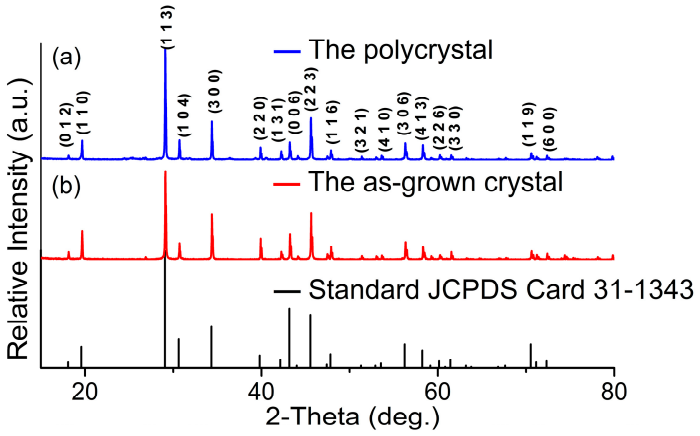

Figure 5. XRPD patterns of $Sr_3(BO_3)_2$ samples. (**a**) Polycrystalline sample and (**b**) single crystal sample.

In order to further determine the phase transition for $Sr_3(BO_3)_2$ crystal, high temperature XRPD measurement was carried out. Figure 6 presents the XRPD patterns of $Sr_3(BO_3)_2$ crystal samples measured from 1150 °C to 1350 °C. It was found from Figure 6a that the main diffraction peaks of $Sr_3(BO_3)_2$ sample were still consistent with the standard data, while some splitting peaks appeared at the diffraction angles (θ) of 28.70°, 34.34°, and 40.02° when the temperature increased above 1250 °C, corresponding to (113), (300), and (220) planes (JCPDS No. 31–1343), respectively. It was found that the diffraction angles (θ) for (113), (300), and (220) planes were all shifted to high angle region then to low angle region, as shown in Figure 6b.

It is known that the relationship between cell parameters and interplanar spacing (d) for crystals with R-3c space group was as follows:

$$\frac{1}{d_{hkl}} = \frac{a^2}{V}\sqrt{\left[(h^2+k^2+l^2)\sin^2\alpha + 2(hk+hl+kl)(\cos^2\alpha - \cos\alpha)\right]}$$

where a, V, and α are cell parameters; h, k, and l are indices of crystal face; and d_{hkl} is the interplanar spacing of (hkl) plane. According to Bragg equation ($2d\sin\theta = n\lambda$), the values of interplanar spacing d for different crystal planes were also related to the diffraction angle θ. Therefore, the variation tendency of 2-Theta could be attributed to the change of d values. Table 1 lists the d_{hkl} values for different crystal planes calculated from XRPD data measured at different temperatures.

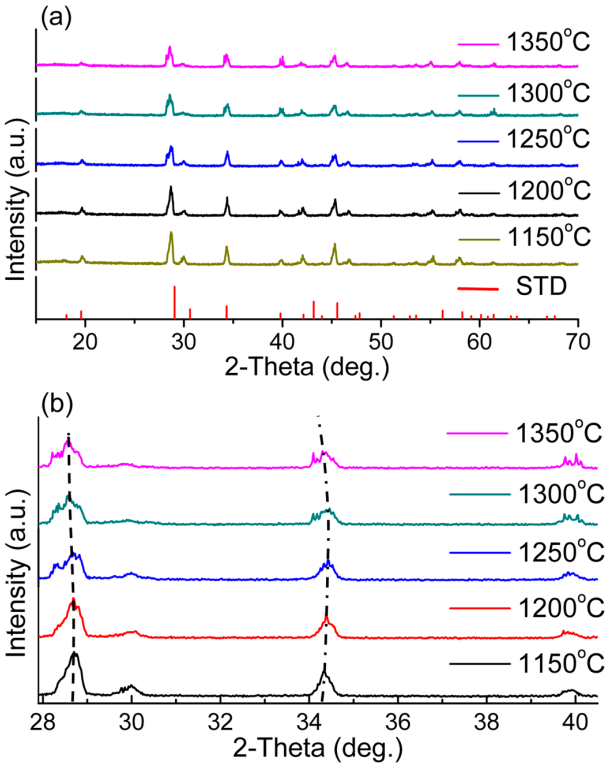

Figure 6. In situ high temperature XRPD results of $Sr_3(BO_3)_2$ crystal (**a**) and the enlarged diffraction pattern ranged from 28° to 41° (**b**).

In order to illustrate the change of crystal structure for $Sr_3(BO_3)_2$, the variations of cell parameters as a function of temperature up to 1350 °C were draw in Figure 7, where a distinct drop was found at 1250 °C. The split of diffraction peaks observed at temperatures above 1250 °C and the significant change of cell parameters at 1250 °C indicating a new crystal phase was formed, which was in accordance with the TG-DTA experimental results. Therefore, the conclusion can be drawn that the endothermic peak in DTA curve observed around 1250 °C should be a reflection of phase transition other than its melting point.

Table 1. Part of cell parameters and interplanar spacing d values of $Sr_3(BO_3)_2$ crystal under different temperatures.

T/°C	1150	1200	1250	1300	1350
a/Å	9.03988	9.04522	9.04469	9.0376	9.04985
b/Å	9.03988	9.04522	9.04469	9.0376	9.04985
c/Å	12.87744	12.87707	12.82442	12.93778	12.96449
V/Å^3	911.35	912.4	908.56	915.16	919.54
d_{113}/Å	3.36251	3.36241	3.34865	3.37827	3.38526
d_{300}/Å	3.71739	3.71728	3.70207	3.73482	3.74254
d_{220}/Å	3.94289	3.94279	3.92664	3.96137	3.96956

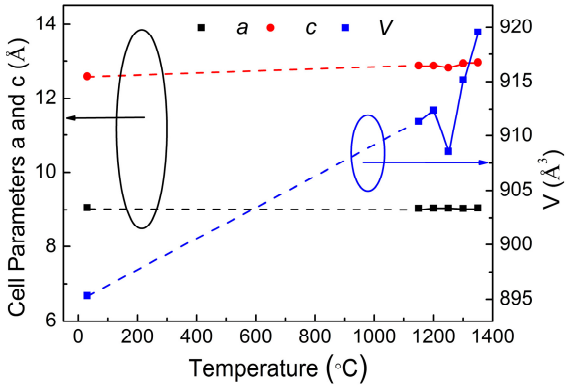

Figure 7. Variation of cell parameters of $Sr_3(BO_3)_2$ as a function of temperature.

4.4. Raman Spectra Analysis

Figure 8 gives the powder Raman spectra of $Sr_3(BO_3)_2$ crystal together with the results of $Ca_3(BO_3)_2$ crystal for comparison. It was noted that the strongest Raman peak for $Sr_3(BO_3)_2$ crystal (900 cm^{-1}) was located at a similar position with that of $Ca_3(BO_3)_2$ crystal (927 cm^{-1}), corresponding to the symmetrical stretching vibration of $[BO_3]^{3-}$. The line widths of the strongest peak were obtained and found to be on the order of 5.72 cm^{-1} and 7.01 cm^{-1} for $Sr_3(BO_3)_2$ and $Ca_3(BO_3)_2$, respectively. On account of the Raman gain coefficient being inversely proportional to the line width [34,35], the $Sr_3(BO_3)_2$ crystal might possess even larger Raman gain than $Ca_3(BO_3)_2$ crystal.

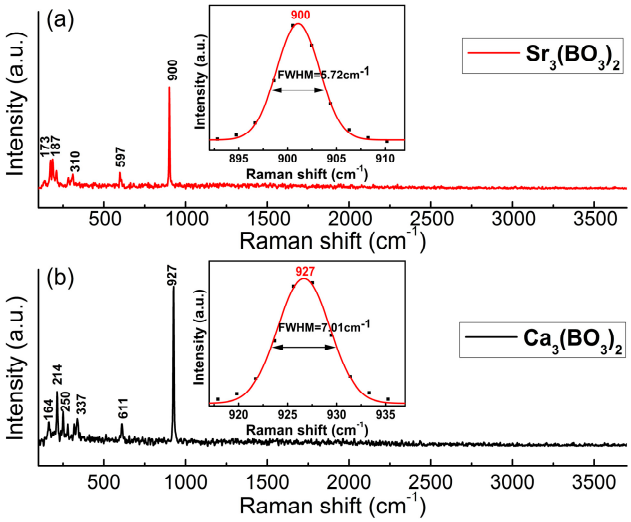

Figure 8. Powder Raman spectra of $Sr_3(BO_3)_2$ crystals (**a**) and $Ca_3(BO_3)_2$ crystals (**b**), the insets were the fitting curves of the strongest Raman peaks.

5. Conclusions

A new kind of Raman crystal $Sr_3(BO_3)_2$ was synthesized by solid state reaction method and Cz pulling method. The crystal structure of $Sr_3(BO_3)_2$ crystal was analyzed by XRPD method and found to possess trigonal symmetry (space group R-3c) similar to $Ca_3(BO_3)_2$. The structure stability was studied by means of TG/DTA and high temperature XRPD up to 1350 °C, where the $Sr_3(BO_3)_2$ crystal was found to show a phase transition around 1250 °C, which induced cracking during crystal cooling. Raman properties were studied theoretically and experimentally, where the $Sr_3(BO_3)_2$ crystal was found to show strong frequency shift at 900 cm^{-1}, comparable to that of $Ca_3(BO_3)_2$ (927 cm^{-1}). In addition, the line width of the strongest Raman peak of $Sr_3(BO_3)_2$ (5.72 cm^{-1}) was lower than $Ca_3(BO_3)_2$ (7.01 cm^{-1}), indicating that $Sr_3(BO_3)_2$ might possess a larger Raman gain coefficient, which is beneficial for the SRS process.

Acknowledgments: This work was supported by the National Natural Science Foundation of China (Grant Nos. 51202129, 51502158, 51372138, 51672160 and 61178060), and The Fundamental Research Funds of Shandong University (2015JC039).

Author Contributions: Xinle Wang and Hongwei Qi contributed to the crystal growth and property characterization work. Yanlu Li carried out the theoretical study on Raman shifts by first principle. Fapeng Yu and Zhengping Wang conceived the experiments. Hewei Wang, Feifei Chen, and Yanqing Liu took part in the single crystal growth. Xinguang Xu and Xian Zhao guided the measurements. All authors contributed in the discussion of experimental results.

Conflicts of Interest: The authors declare no conflict of interest.

References

1. Li, Y.L.; Ye, Y.; Fan, Y.D.; Zhou, J.; Jia, L.; Tang, B.; Wang, X.G. Silver nanoprism-loaded eggshell membrane: a facile platform for in situ sers monitoring of catalytic reactions. *Crystals* **2017**, *7*, 45. [CrossRef]
2. Saar, B.G.; Freudiger, C.W.; Reichman, J.; Stanley, C.M.; Holtom, G.R.; Xie, X.S. Video-rate molecular imaging in vivo with stimulated raman scattering. *Science* **2010**, *330*, 1368–1370. [CrossRef] [PubMed]
3. Girlando, A.; Masino, M.; Brillante, A.; Toccoli, T.; Iannotta, S. Raman identification of polymorphs in pentacene films. *Crystals* **2016**, *6*, 41. [CrossRef]
4. Du, Y.; Cai, Q.; Xue, J.D.; Zhang, Q. Raman and terahertz spectroscopic investigation of cocrystal formation involving antibiotic nitrofurantoin drug and coformer 4-aminobenzoic acid. *Crystals* **2016**, *6*, 164. [CrossRef]
5. Lioe, D.X.; Mars, K.; Kawahito, S.; Yasutomi, K.; Kagawa, K.; Yamada, T.; Hashimoto, M. A stimulated raman scattering CMOS pixel using a high-speed charge modulator and lock-in amplifier. *Sensors* **2016**, *16*, 532. [CrossRef] [PubMed]
6. Wang, W.J.; Guo, M.; Lu, D.L.; Wang, W.M.; Fu, Z.Y. Effect of HNO3 concentration on the morphologies and properties of Bi_2WO_6 photocatalyst synthesized by a hydrothermal method. *Crystals* **2016**, *6*, 75. [CrossRef]
7. Wu, D.; Huang, H.; Zhu, X.P.; He, Y.W.; Xie, Q.L.; Chen, X.L.; Zheng, X.M.; Duan, H.G.; Gao, Y.L. E" Raman Mode in Thermal Strain-Fractured CVD-MoS_2. *Crystals* **2016**, *6*, 151. [CrossRef]
8. Wu, Z.X.; Wang, Z.P.; Zhang, F.; Liu, Y.Q.; Lu, J.R.; Xu, X.G. Optical frequency fork based on stimulated Raman scattering. *J. Alloys Compd.* **2016**, *682*, 537–542. [CrossRef]
9. Bergmann, V.; Meier, W.; Wolff, D.; Stricker, W. Application of spontaneous Raman and Rayleigh scattering and 2D LIF for the characterization of a turbulent $CH_4/H_2/N_2$ jet diffusion flame. *Appl. Phys. B* **1998**, *66*, 489–502. [CrossRef]
10. Cavalcante, L.S.; Sczancoski, J.C.; Lima, L.F., Jr.; Espinosa, J.W.M.; Pizani, P.S.; Varela, J.A.; Longo, E. Synthesis, characterization, anisotropic growth and photoluminescence of $BaWO_4$. *Cryst. Growth Des.* **2009**, *9*, 1002–1012. [CrossRef]
11. Ivleva, L.I.; Voronina, I.S.; Lykov, P.A.; Berezovskaya, L.Y.; Osiko, V.V. Growth of optically homogeneous $BaWO_4$ single crystals for Raman lasers. *J. Cryst. Growth* **2007**, *304*, 108–113. [CrossRef]
12. Zvereva, P.G.; Basieva, T.T.; Osikoa, V.V.; Kulkovb, A.M.; Voitsekhovskiib, V.N.; Yakobsonb, V.E. Physical, chemical and optical properties of barium nitrate Raman crystal. *Opt. Mater.* **1999**, *11*, 315–334. [CrossRef]

13. Li, X.L.; Lee, A.J.; Huo, Y.J.; Zhang, H.J.; Wang, J.Y.; Piper, J.A.; Pask, H.M.; Spence, D.J. Managing SRS competition in a miniature visible Nd:YVO_4/$BaWO_4$ Raman laser. *Opt. Express* **2012**, *20*, 19305–19312. [CrossRef]
14. Kaminskii, A.A.; Ueda, K.; Eichler, H.J.; Kuwano, Y.; Kouta, H.; Bagaev, S.N.; Chyba, T.H.; Barnes, J.C.; Gad, G.M.A.; Murai, T.; et al. Tetragonal vanadates YVO_4 and $GdVO_4$—New efficient $\chi^{(3)}$—Materials for Raman lasers. *Opt. Commun.* **2001**, *194*, 201–206. [CrossRef]
15. Chen, Y.F. Compact efficient all-solid-state eye-safe laser with self-frequency Raman conversion in a Nd:YVO_4 crystal. *Opt. Lett.* **2004**, *29*, 2172–2174. [CrossRef] [PubMed]
16. Hammond, R.B.; Orley, M.J.; Roberts, K.J.; Jackson, R.A.; Quayle, M.J. An examination of the influence of divalent cationic dopants on the bulk and surface properties of $Ba(NO_3)_2$ associated with crystallization. *Cryst. Growth Des.* **2009**, *9*, 2588–2594. [CrossRef]
17. Yu, H.H.; Hu, D.W.; Zhang, H.J.; Wang, Z.P.; Ge, W.W.; Xu, X.G.; Wang, J.Y.; Shao, Z.S.; Jiang, M.H. Picosecond stimulated Raman scattering of $BaWO_4$ crystal. *Opt. Laser Technol.* **2007**, *39*, 1239–1242. [CrossRef]
18. Liu, Y.Q.; Zhang, F.; Wang, Z.P.; Yu, F.P.; Wei, L.; Xu, X.G.; Zhao, X. $Ca_3(BO_3)_2$, a first wide waveband borate Raman laser crystal with strong Raman effects and outstanding anti-optical damage ability. *J. Mater. Chem. C* **2015**, *3*, 10687–10694. [CrossRef]
19. Porto, S.P.S.; Scott, J.F. Raman spectra of $CaWO_4$, $SrWO_4$ $CaMoO_4$ and $SrMoO_4$. *Phys. Rev.* **1967**, *157*, 716–719. [CrossRef]
20. Černýa, P.; Zverevb, P.G.; Jelínkováa, H.; Basievb, T.T. Efficient Raman shifting of picosecond pulses using $BaWO_4$ crystal. *Opt. Comm.* **2000**, *177*, 397–404. [CrossRef]
21. Basiev, T.T.; Sobol, A.A.; Voronko, Y.K.; Zverev, P.G. Spontaneous Raman spectroscopy of tungstate and molybdate crystals for Raman lasers. *Opt. Mater.* **2000**, *15*, 205–216. [CrossRef]
22. Goldschmidt, V. M. Die Gesetze der Krystallochemie. *Naturwissenschaften* **1926**, *14*, 477–485. [CrossRef]
23. Shannon, R.D. Revised effective ionic radii and systematic studies of interatomic distances in halides and chalcogenides. *Acta. Cryst.* **1976**, *A32*, 751–767. [CrossRef]
24. Wang, H.Y.; Jia, G.H.; Wang, Y.; You, Z.Y.; Li, J.F.; Zhu, Z.J.; Yang, F.G.; Wei, Y.P.; Tu, C.Y. Crystal growth and spectral properties of pure and Co^{2+}-doped $Mg_3B_2O_6$ crystal. *Opt. Mater.* **2007**, *29*, 1635–1639. [CrossRef]
25. Richter, L.; Muller, F. Zur Struktur von $Sr_3B_2O_6$. *Z. Anorg. Allg. Chem.* **1980**, *467*, 123–125. [CrossRef]
26. International Centre of Diffraction Data (ICDD). PCPDF 31–1343. Available online: http://www.icdd.com (accessed on 10 March 2017).
27. International Centre of Diffraction Data (ICDD). PCPDF 38–1475. Available online: http://www.icdd.com (accessed on 10 March 2017).
28. Segall, M.; Lindan, P.; Probert, M.; Pickard, C.; Hasnip, P.; Clark, S.; Payne, M. First-principles simulation: ideas, illustrations and the CASTEP code. *J. Phys. Condens. Matter* **2002**, *14*, 2717–2744. [CrossRef]
29. Perdew, J.P.; Burke, K.; Ernzerhof, M. Generalized gradient approximation made simple. *Phys. Rev. Lett.* **1996**, *77*, 3865–3868. [CrossRef] [PubMed]
30. Vanderbilt, D. Soft self-consistent pseudopotentials in a generalized eigenvalue formalism. *Phys. Rev. B* **1990**, *41*, 7892–7895. [CrossRef]
31. Fletcher, J.G.; Glasser, F.P. Phase relations in the system CaO-B_2O_3-SiO_2. *J. Mater. Sci.* **1993**, *28*, 2677–2686. [CrossRef]
32. Barseghyan, A.H.; Hovhannisyan, R.M.; Petrosyan, B.V.; Aleksanyan, H.A.; Toroyan, V.P. Glass formation and crystalline phases in the ternary systems CaO-Bi_2O_3-B_2O_3 and SrO-Bi_2O_3-B_2O_3. *Phys. Chem. Glasses* **2013**, *54*, 199–205.
33. Liang, G.; Tang, Z.; Fang, H.; Katz, D.; Salama, K. Synthesis and X-ray diffraction pattern for $MgCu_2$. *J. Alloys Comp.* **2006**, *422*, 73–77. [CrossRef]
34. Piper, J.A.; Pask, H.M. Crystalline Raman Lasers. *J. Sel. Top. Quant.* **2007**, *13*, 692–704. [CrossRef]
35. Pask, H.M. The design and operation of solid-state Raman lasers. *Prog. Quant. Electron.* **2003**, *27*, 3–56. [CrossRef]